HIGH-RESOLUTION, REAL-TIME X-RAY IMAGING SYSTEM USING SYNCHROTRON RADIATION FOR ANIMAL STUDIES

K. Umetani*, M. Kobatake**, A. Yamamoto**, T. Yamashita**, S. Imai** and Y. Kajihara**

* Japan Synchrotron Radiation Research Institute/Research & Utilization Division, Hyogo, Japan
** Kawasaki Medical School/Department of Diagnostic Radiology, Okayama, Japan

umetani@spring8.or.jp

Abstract: An X-ray direct-conversion type detector with spatial resolutions of ca. 6 and 10 μm was developed for real-time biomedical imaging. The detector was composed of an X-ray direct-conversion type SATICON pickup tube. The X-ray image is converted directly into an electric signal in the photoconductive layer without image blur. In synchrotron radiation radiography, a long source-to-object distance and a small source spot can produce high-resolution images. Using the direct-conversion type detector and the synchrotron radiation source at SPring-8, microangiography experiments were carried out for depicting tumor angiogenic vessels in a rabbit model of cancer.

Introduction

Medical imaging using synchrotron radiation has been investigated since intravenous coronary angiography research was begun in the late 1970s for its potential to provide safer intravenous angiography technique to replace conventional selective coronary arteriography [1–6]. An intra-arterial high-resolution microangiography system was developed for preclinical animal studies in addition to intravenous diagnostic imaging [7]. Subsequently, we developed a new digital microangiography system with spatial resolution to 10 μm for *in vivo* animal studies. In this system, an X-ray direct-conversion type detector incorporating an X-ray SATICON pickup tube was employed for preclinical testing using tumor-bearing animals [8].

The first X-ray direct-conversion type pickup tube was developed in the 1960s using a PbO photoconductive material. The direct-conversion type detector was combined with a high-power X-ray generator for observing real-time topography images in material science fields. Photoconductive materials were improved for high-resolution imaging. In place of the PbO photoconductive material, the X-ray SATICON tube with an amorphous photoconductive Se-As alloy target was developed for use in synchrotron radiation experiments of live topography at the Photon Factory [9].

The new X-ray SATICON camera for medical imaging was much improved through introduction of a high-definition television system, which increased resolution to 1050 scanning lines (Hamamatsu Photonics K.K. and Hitachi Techno-System Ltd.). The camera can take images at a maximum rate of 30 images/s. Sequential images were obtained with an input field of view of 9.5 mm × 9.5 mm. Digital images were stored in a digital-image acquisition system after analog-to-digital conversion, synchronizing timing with electron beam scanning in the pickup tube [8]. The system has been improved with respect to spatial resolution by zooming in an object; the input field of view was reduced to 4.5 mm × 4.5 mm for higher spatial resolution imaging with resolution to 6 μm for depicting tumor angiogenic small vessels in a rabbit model of cancer [10].

Materials and Methods

The camera system shown in Fig. 1 comprises a camera head incorporating the X-ray SATICON pickup tube and a camera control unit with an analog-to-digital converter for digital signal output. X-rays enter the SATICON tube through an aluminum window. As shown in Fig. 2, absorbed X-rays in the photoconductive layer are directly converted into electron-hole pairs. Charge carriers generated by X-rays are transported across the photoconductive layer by an electric field. Then, a charge-density pattern is formed on the photoconductive layer surface. The electrostatic image on the surface is read out by a scanning beam of low velocity electrons to produce a video signal.

Figure 1: Photograph of the X-ray SATICON camera system consisting of a camera head (left) and a camera control unit (right)

The principal elements of the camera heads in Fig. 1 are the SATICON tube, electron beam scanning and focusing coils, and operation electronics. The electron

ISSN: 1727-1983

beam scans the surface of the photoconductive layer in a raster fashion. The input field of view is defined by the beam scanning area in Fig. 2. In a normal imaging mode with the detector's input field of view of 9.5 mm × 9.5 mm, an equivalent pixel size is 9.5 μm in the case of a 1024 × 1024-pixel format. On the other hand, in a zoom imaging mode, the input field is 4.5 mm × 4.5 mm with pixel size of 4.5 μm.

In Fig. 2, X-ray absorption depends on the photoconductive layer thickness. Thickness of amorphous selenium is 25 μm, yielding a detection efficiency of 14.2% for 33.2 keV X-rays.

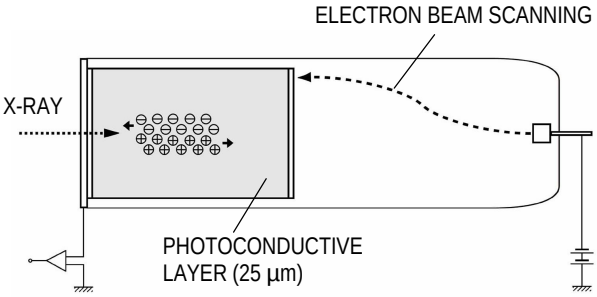

Figure 2: Schematic cross-section of the SATICON tube

The camera can take sequential images at a maximum speed of 30 images/s. Then the image signals are converted to digital data with the 1024 × 1024-pixel and 10-bit format by an analog-to-digital converter installed in the camera control unit shown in Fig. 1. Digital images are stored in 2 GB RAM of a custom-designed frame memory system after analog-to-digital conversion (SR-DR-7; Zenisu Keisoku Inc.). Image storage is synchronized with electron beam scanning in the pickup tube. A personal computer system controls the entire imaging system, including the camera control unit and the frame memory system.

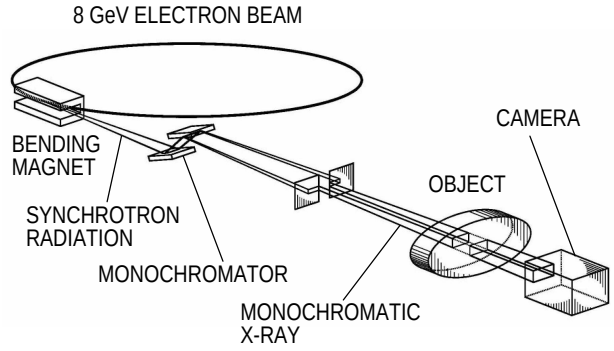

Figure 3: Illustration of the experimental arrangement

In vivo imaging experiments were performed at the SPring-8 BL20B2 bending-magnet beamline. Figure 3 shows the experimental arrangement for X-ray imaging using monochromatic synchrotron radiation X-rays. Synchrotron radiation has a broad and continuous spectrum, extending from the infrared to the X-ray region. A double crystal monochromator selects a single energy of synchrotron radiation. X-rays transmitted through an object are detected by the X-ray SATICON camera.

The beamline's full length is 215 m from the X-ray source to the end station. The first and second experimental hutches are located 42 and 206 m from the source point; imaging experiments were performed respectively in zoom and normal imaging modes of the detector. A nearly parallel X-ray beam is used for imaging without geometrical image blur because of the small size of the X-ray source and the very long source-to-object distance.

The storage ring was operated with 8 GeV electron beam energy and 80–100 mA beam current. Monochromatic X-ray energy was adjusted to 33.2 keV, just above the iodine K-edge energy, in the normal imaging mode. X-ray energy was adjusted to 13.0 keV in the zoom mode to produce a higher-contrast image of the iodine contrast agent than that at 33.2 keV.

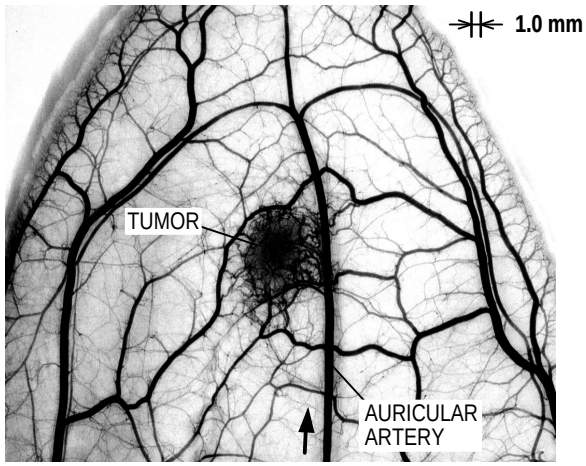

Figure 4: X-ray film image of a tumor-implanted rabbit auricle specimen

A tumor stimulates the growth of small blood vessels for feeding the tumor itself. It has been proposed that tumor-induced small vessels are an intrinsic part of tumor development and progression. The growth rate of tumors is slow before blood vessel formation and rapid after the vessel formation [11–13]. In a conventional angiography technique, a rabbit auricle specimen implanted with VX2 carcinoma is fixed with formalin after a barium sulfate solution is injected into the auricular artery as a contrast agent [14]. Figure 4 shows a radiographic image of a rabbit auricle specimen taken using a conventional X-ray tube and film/screen system with spatial resolution of ca. 30 μm. A black arrow shows the direction of blood flow. The tumor shows a hypervascular lesion in the center of the auricle; vessels are much more numerous there than in normal areas.

In this study, *in vivo* imaging of tumor angiogenic vessels was performed with spatial resolutions higher than that of conventional specimen imaging shown in Fig. 4. The VX2 carcinoma is a rapidly growing solid

ISSN: 1727-1983

tumor. Tumor cells are transplanted easily into other rabbits. Japanese white rabbits weighing about 3 kg were used for microangiographic imaging. Rabbits were anesthetized by intravenous injection of sodium pentobarbital. The VX2 cancer cells were subcutaneously injected into the rabbit auricle.

Microangiography experiments were performed at 1–7 days after transplantation. Rabbits were similarly anesthetized. The contrast agent was injected into the auricular artery using a mechanical power injector. Volume of the contrast agent was 2.4 ml per injection at a speed of 0.2 ml/s. Images were obtained sequentially at 3.75 images/s; the exposure time for each image was 0.27 s. Sequential images were stored in the frame memory system with 10-bit resolution and 1024 × 1024-pixel format. All animal experiments conformed to the SPring-8 Guide for Care and Use of Laboratory Animals.

Results

Performance of the direct-conversion type detector was evaluated by taking images of custom-designed gold resolution charts. Thicknesses of the charts were 23 and 5 μm; their respective bar pattern widths were 8.8–31.4 and 5.0–12.1 μm. Figure 5 shows an X-ray image of the 23-μm-thick chart taken in the normal imaging mode of the detector with the field of view of 9.5 mm × 9.5 mm at an X-ray energy of 33.2 keV. The numerical values in Fig. 5 show bar widths. In the chart image, the 11.8-μm-wide bars are visible. The limiting spatial resolution is around 10 μm because the 11.8-μm bars are readily visible in the image.

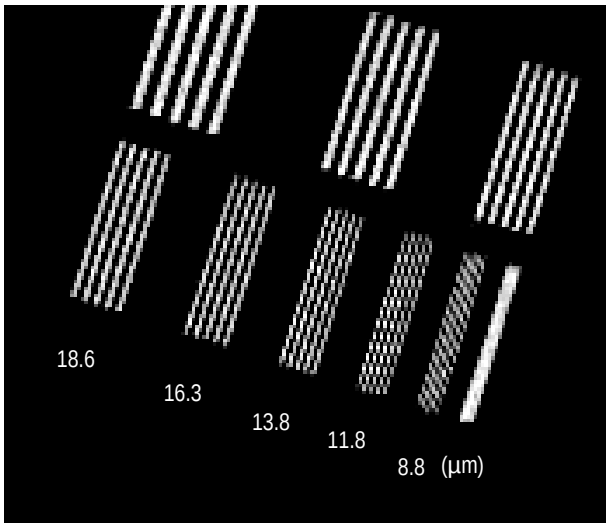

Figure 5: X-ray image of the central area of the 23-μm-thick chart

An image of another chart with micrometer-sized bar patterns was obtained in the zoom imaging mode of the detector with a 4.5 mm × 4.5 mm field of view at an X-ray energy of 20.0 keV. Figure 6 shows an image of the 5-μm-thick chart; the 6.0-μm-wide bars are visible. The limiting spatial resolution is about 6.0 μm in the zoom imaging mode. The 6.0 μm bar width is comparable with the size of the capillary blood vessels.

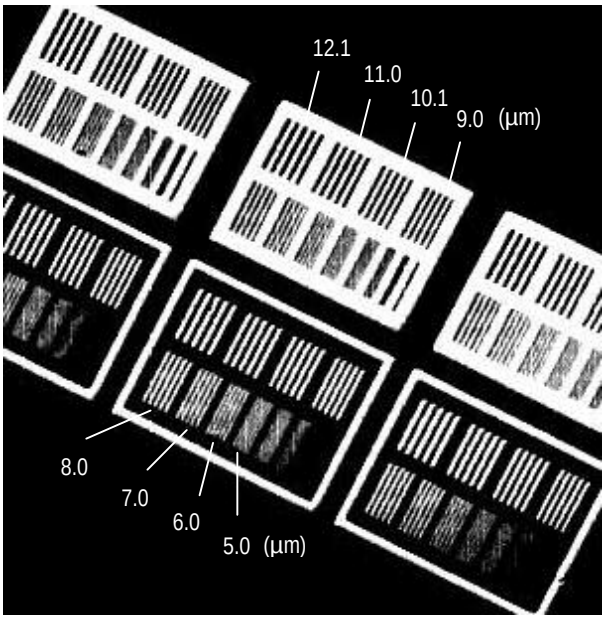

Figure 6: X-ray image of the central area of the 5-μm-thick chart

Representative images of blood vessels in the same rabbit auricle are shown in Fig. 7. Images from microangiographic sequences were taken using (a) 33.2-keV X-rays in the normal imaging mode and (b) 13.0-keV in the zoom mode at one day after tumor transplantation. Figure 7(b) corresponds to a magnified image of the dotted rectangular area in Fig. 7(a); that image can display microscopic angioarchitecture.

Each image in Fig. 7 depicts a summation result of four consecutive frames in the microangiographic sequence; the exposure time was 1.07 s. Original frames, however, were obtained at a rate of 3.75 frames per second and exposure time of 0.27 s. Image summation was required to increase the signal-to-noise ratio and to detect small blood vessels. In addition, a temporal subtraction operation was performed for flat-field correction using summation results of four consecutive frames acquired before contrast-agent injection. The summation image taken before injection was subtracted from raw images taken after injection to eliminate the superimposed background structure.

Immediately after iodine-contrast-agent injection to the auricular artery, the microangiography system mainly showed the network of normal and tumor-angiogenic arteries originating from branches of the auricular artery. Then the network of normal and tumor-angiogenic veins gradually became visible. Both the arteries and veins finally showed the highest contrast. Images in Fig. 7 were obtained at the same opacifying timing of the flow of contrast agent, where both the arteries and veins have the highest contrast.

ISSN: 1727-1983

As the tumor grows, it might come to encase normal blood vessels, thereby causing vascular stenosis and flow disturbances. When the tumor encases the vessel, a sharp demarcation between the vessel and the tumor is often visible. Two black arrows in each image in Fig. 7 indicate vascular stenosis and occlusion in the normal blood vessels, where the tumor cells were vital and the tumor's growth rate was rapid at one day after tumor transplantation.

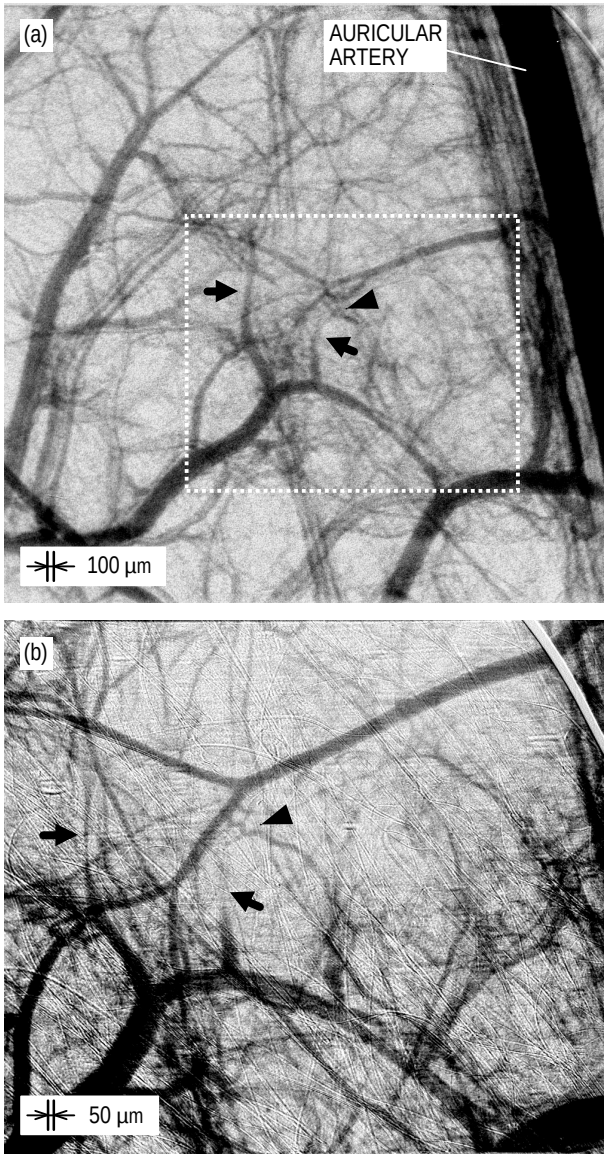

Figure 7: Angiographic images of the rabbit auricle taken using (a) normal and (b) zoom imaging modes

The tumor angiogenic blood vessels exhibit numerous irregular arteries and veins, which have the characteristic appearance of an undulating shape lacking side branches. In the high-resolution image shown in Fig. 7(b), a black arrowhead shows one angiogenic vessel that has an undulating shape lacking side branches. In Fig. 7(a), a black arrowhead shows the same angiogenic vessel, but it does not demonstrate the undulating shape because of lower contrast and resolution.

Discussion

The image in Fig. 7(a) was taken using 33.2-keV X-rays, which are useful for diagnostic imaging. On the other hand, the image in Fig. 7(b) was produced by 13.0-keV X-rays to obtain a higher contrast image than that by 33.2-keV X-rays. The X-ray mass attenuation coefficient of iodine at 13.0 keV is 2.5 times larger than that at 33.2-keV. However, low energy X-rays are applicable only to small parts of animal bodies – rabbit auricles, rodent extremities, and rodent tails – for high-resolution and high-contrast imaging. The microangiography system is applicable to widely various animal body parts and organs for preclinical testing using the combination of two imaging modes and two X-ray energies.

Light microscopes are widely used for conventional *in vivo* preclinical studies. However, the depth of the viewing field in focus is restricted to sub-micrometer to micrometer ranges. On the other hand, because of the very large depth of field, an X-ray micro-imaging system using a nearly parallel synchrotron radiation beam offers advantages over light microscopes for imaging of internal structures of centimeter-sized thick objects with spatial resolution in the micrometer range.

In imaging of the spatial resolution chart, the 6.0-µm-wide bars are visible in Fig. 6. The limiting spatial resolution is about 6.0 µm in the zoom imaging mode with the field of view of 4.5 mm × 4.5 mm. The 6.0 µm bar width is comparable with the size of the capillary blood vessels. If capillaries are opacified using a high-density contrast agent, images of the capillaries are obtainable using low energy X-rays [15]. However, the contrast agent is diluted substantially in the blood flow before it enters the tumor angiogenic vessels. In Fig. 7(b), blood vessels of around 20 µm diameter were observed as the smallest vessels.

Images shown in Fig. 7 were obtained at the same opacifying timing as the flow of contrast agent, where both the arteries and veins offer the highest contrast. On the other hand, immediately after injection of the contrast agent to the auricular artery, the microangiography system shows only the network of arteries originating from the branches of the auricular artery. Solely at the time of opacifying the arteries can the imaging system visualize arteries with diameters less than 20 µm. At that time, the arteries are the sole object on the uniform background [10].

Regarding angioarchitecture, the tumor's growth in its initial stage exhibits myriad characteristic appearances of normal and tumor-angiogenic blood vessels at the time when both the arteries and veins have the highest contrast in Fig. 7. On the contrary, after the tumor's full growth, numerous blood vessels overlap considerably and individual blood vessels become unidentifiable, as shown in Fig. 4. The initial stage of tumor growth provides a useful tool for observation of

ISSN: 1727-1983

the appearance and transformation of blood vessels. The tumor itself is not shown in Fig. 7, but vascular stenosis and occlusion in the normal blood vessels and the angiogenic vessels' undulating shape indicate the tumor size at one day after tumor transplantation.

Conclusions

The synchrotron radiation microangiography system allows depiction of normal and tumor-derived small blood vessels in animal studies using 33.2 and 13.0 keV monochromatic X-rays and two imaging modes with fields of view of 9.5 mm × 9.5 mm and 4.5 mm × 4.5 mm. The imaging system revealed that the tumor's growth in its initial stage shows many aspects of the characteristic appearance of normal and tumorous angiogenic blood vessels at the time when both the arteries and veins have the highest contrast. Blood vessels of around 20 μm diameter are visible as the smallest vessels.

The synchrotron radiation system is a useful tool for evaluating the micro-angioarchitecture of malignant tumors in animal models of cancer. *In vivo* preclinical studies can be performed using the rabbit model of cancer for testing of anticancer drugs, embolization materials in transcatheter arterial embolization, radiation therapy, and so on using the microangiographic technique. Sequential changes in angiogenic vessels can be determined in these types of treatments. The microangiographic approach might precisely evaluate the effect of cancer treatment and the level of cancer treatment.

Acknowledgements

The authors wish to thank Mr. Tadaaki Hirai and Mr. Toshiaki Kawai of Hamamatsu Photonics KK, Mr. Sadao Takahashi of Hitachi Denshi Techno-System, Ltd., and Mr. Norio Iwanaga of Zenisu Keisoku Inc. for development of the camera and frame memory system. Synchrotron radiation experiments were performed at the SPring-8 BL20B2 beamline with the approval of the Japan Synchrotron Radiation Research Institute (Acceptance Nos. 2003B0186-NL3-np, 2004A0527-NL3-np, and 2004B0004-NL3-np).

References

[1] RUBENSTEIN E., HOFSTADTER R., ZEMAN H.D., THOMPSON A.C., OTIS J.N., BROWN G.S., GIACOMINI J.C., GORDON H.J., KERNOFF R.S., HARRISON D.C., and THOMLINSON W. (1987): 'Transvenous Coronary Angiography in Human Using Synchrotron Radiation', *Proc. Natl. Acad. Sci. U.S.A.*, **83**, pp. 9724-9728

[2] THOMLINSON W. (1996): 'Transvenous Coronary Angiography in Humans', in BURATTINI E. and BALERNA A. (eds.): 'Proc. the International School of Physics "Enrico Fermi," Course CXXVIII, Biomedical Applications of Synchrotron Radiation', (IOS Press, Amsterdam), pp. 127-153

[3] DIX W.-R., GRAEFF W., HEUER J., ENGELKE K., JABS H., KUPPER W., and STELLMASCHEK K.H. (1989): 'NIKOS II–A System for Noninvasive Coronary Angiography with Synchrotron Radiation', *Rev. Sci. Instrum.*, **60**, p. 2260

[4] DILL, T., DIX, W.-R., HAMM, C.W., JUNG, M., KUPPER, W., LOHMANN, M., REIME, B., and VENTURA, R. (1998): 'Intravenous Coronary Angiography: Experience in 276 Patients', *Synchrotron Radiation News*, **11**(2), pp. 12-20

[5] OHTSUKA S., SUGISHITA Y., TAKEDA T., ITAI Y., HYODO K., and ANDO M. (1997): 'Dynamic Intravenous Coronary Arteriography Using Synchrotron Radiation and Its Application to the Measurement of Coronary Blood Flow', *Jpn. Circ. J.*, **61**(5), pp. 432-440

[6] ELLEAUME H., FIEDLER S., ESTÈVE F., CHARVET A. M., BERTRAND B., BERKVENS P., BERRUYER G., BROCHARD T., LE DUC G., NEMOZ C., RENIER M., SUORTTI P., THOMLINSON W., and LE BAS J. F. (2000): 'First Human Transvenous Coronary Angiography at the European Synchrotron Radiation Facility', *Phys. Med. Biol.*, **45**, pp. L39-L43

[7] UMETANI K., UEKI H., TAKEDA T., ITAI Y., MORI H., TANAKA E., UDDIN-MOHAMMED M., SHINOZAKI Y., AKISADA M., and SASAKI Y. (1998): 'High-Spatial-Resolution and Real-Time Medical Imaging Using a High-Sensitivity HARPICON Camera', *J. Synchrotron Rad.*, **5**, pp. 1130-1132

[8] UMETANI K., YAMASHITA T., MAEHARA M., IMAI S., and KAJIHARA Y. (2001): 'Synchrotron Radiation Microangiography for Real-Time Observation of Angiogenic Vessels in Cancer', *Anal. Sci.*, **17** Supp., pp. i531-i534

[9] CHIKAWA J., SATO F., KAWAMURA T., KURIYAMA T., YAMASHITA T., and GOTO N. (1986): 'A High-Resolution Video Camera Tube for Live X-Ray Topography Using Synchrotron Radiation', in HOSOYA S. *et al.* (eds.): 'X-ray Instrumentation for the Photon Factory: Dynamic Analysis of Micro Structures in Matter', (KTK Scientific Publishers, Tokyo), pp. 145-157

[10] UMETANI K., YAMASHITA T., MAEHARA N., TOKIYA R., IMAI S., and KAJIHARA Y. (2003): 'Small-Field Angiographic Imaging of Tumor Blood Vessels in Rabbit Auricle Using X-ray SATICON Camera and Synchrotron Radiation', Proc. of 25th Annual Int. Conf. of the IEEE Engineering in Medicine and Biology Society, Mexico, 2003, pp. 978-981

[11] FOLKMAN J. (1972): 'Anti-Angiogenesis: New Concept for Therapy of Solid Tumors', *Ann. Surg.*, **175**, pp. 409-416

[12] FOLKMAN J. (1990): 'What is the Evidence that Tumors are Angiogenesis Dependent?', *J. Natl. Cancer Inst.*, **82**, pp. 4-6

ISSN: 1727-1983

[13] FOLKMAN J. (1995): 'Angiogenesis in Cancer, Vascular, Rheumatoid and Other Disease', *Nat. Med.*, **1**, pp. 27-31

[14] YAMASHITA T. (2001): 'Evaluation of the Microangioarchitecture of Tumors by use of Monochromatic X-Rays', *Invest. Radiol.*, **36**, pp. 713-720

[15] UMETANI K., ITASAKA S., OGURA M., KIMURA H., and HIRAOKA M. (2001): 'Synchrotron Radiation Microangiography System for Observation of Blood Flow in Murine Tumor Vasculature', *Bioimages*, **9**, pp. 97-106

ISSN: 1727-1983